ISSN (Print) 1226-1750
ISSN (Online) 2233-6656
Journal of Magnetics 31(3), 416-423 (2026) https://doi.org/10.4283/JMAG.2026.31.3.416

Multi-Parameter Optimization of RF Relay Performance via the Kriging-Improved Adaptive Genetic Algorithm Hybrid Approach

Chaoqun Cheng[1], Jiaxin You[1], Xinyu Jin[1]*, Lingzhi Wang[2], Aobo Wang[1], and Le Xu[1]

[1]*Institute of Reliability in Electrical Apparatus and Electronics, Harbin Institute of Technology, Harbin 150001, China*
[2]*Xiamen Hongfa Electroacoustic CO., LTD., Xiamen 361021, China*

(Received 31 December 2025, Received in final form 1 July 2026, Accepted 13 July 2026)

Radio frequency electromagnetic relays are critical for signal transmission in aerospace applications but face significant challenges in reducing insertion loss, particularly due to the magnetic hysteresis and eddy current losses inherent in their ferromagnetic materials under high-frequency excitation. This paper proposes a multi-parameter optimization framework to enhance RF performance by effectively shielding the magnetic layer. Integrating HFSS simulation, Kriging surrogate models, and experimental validation, the study optimizes both macroscopic structural parameters and microscopic material processes. Specifically, the grain texture formed by magnetron sputtering is implicitly optimized to minimize skin depth and confine high-frequency currents to the non-magnetic coating. A hybrid method combining Kriging interpolation and an Improved Adaptive Genetic Algorithm is proposed to overcome the multi-parameter nonlinear coupling effects. Experimental results demonstrate that the optimized relay achieves an insertion loss of <1.8 dB at 5 GHz, with a 23.04% improvement at the primary operating frequency. This work validates a methodology for optimizing high-frequency magnetic devices by bridging material microstructure control with geometric design.

Keywords : RF relay, insertion loss, Kriging model, genetic algorithm

1. Introduction

Insertion loss is closely related to electromagnetic shielding effectiveness and serves as a key indicator for assessing the electromagnetic shielding capability of materials or structures. Essentially, insertion loss measures the reduction in electromagnetic field coupling when a shielding material is placed between the transmitter and the receiver [1]. According to the classical Schelkunoff theory [2], the electromagnetic interference shielding effectiveness (EMI SE) consists of three components: reflection loss, absorption loss, and multiple reflection loss. Insertion loss is essentially another expression of the total shielding effectiveness.

Insertion loss is a key performance index for high-frequency systems [3]. RF electromagnetic relays switch RF signal paths through electromagnetic actuation and are widely used in radar, electronic countermeasures, communication satellites, and measurement instruments [4, 5]. Their insertion loss is strongly affected by material properties, grain structure, and contact geometry [6, 7]. Manual parameter tuning is inefficient for such coupled high-frequency problems; therefore, automated optimization methods are increasingly used to improve RF relay design efficiency and performance [8, 9].

Kriging surrogate models are effective for electromagnetic optimization because they approximate nonlinear relationships between RF performance and geometric or material variables while reducing the number of expensive full-wave simulations [10-12]. Previous studies have used Kriging models for electromagnetic device design, sensitivity-based parameter selection, and uncertainty quantification [13-15]. However, an efficient global optimizer is still required when the design space contains multiple coupled variables.

Genetic algorithms (GAs) provide global search capability and have been applied to RF component optimization [16, 17]. Coupling GA with a Kriging surrogate reduces the cost of evaluating candidate solutions and helps avoid local optima [18]. However, convergence speed and parameter settings remain important limitations in complex multi-parameter problems [19].

©The Korean Magnetics Society. All rights reserved.
*Corresponding author: Tel: +8615362001374
Fax: +86-451-86413964, E-mail: 24S106093@stu.hit.edu.cn

© 2026 Journal of Magnetics

To address these limitations, this study proposes a hybrid optimization method that combines Kriging interpolation with an improved adaptive genetic algorithm (IAGA) for RF relays. The method is designed to overcome the limitations of traditional single-factor analysis when nonlinear coupling exists among multiple parameters.

2. Theory and Analysis

2.1. Kriging Surrogate Model

The insertion-loss curve of an RF relay varies irregularly with frequency, but parameter changes produce repeatable response trends. As illustrated in Fig. 1 for spring width, these trends can be learned by a Kriging surrogate, reducing repeated HFSS simulations.

The Kriging surrogate establishes a mapping y: Rm to R between design variables and response. It includes a deterministic polynomial trend and a stochastic residual term, with the covariance function describing spatial correlation among samples. The assumed form is:

$$G(x)=\sum_{h=1}^{p}\beta_h g_h(x)+z(x)=g^{\mathrm{T}}(x)\beta+z(x) \tag{1}$$

where $g(x)$ is the polynomial function of the independent variable x, expressed as $g(x) = [g_1(x),\cdots, g_p(x)]^{\mathrm{T}}$; β represents the regression coefficients corresponding to $g(x)$, expressed as $\beta=[\beta 1,\cdots, \beta p]^{\mathrm{T}}$; $z(x)$ is the variance function with a mean of 0, and its covariance is:

$$Cov[z(x_i),z(x_j)]=\sigma^2 R(x_i,x_j;\theta) \tag{2}$$

where σ is the standard deviation, and $R(\boldsymbol{xi}, \boldsymbol{xj}; \theta)$ is the correlation coefficient of $z(\boldsymbol{xi})$, $z(\boldsymbol{xj})$, and θ which is the n×n positive definite covariance matrix.

$$R=\begin{pmatrix} r(x_1,x_2) & \cdots & r(x_1,x_n) \\ \vdots & \ddots & \vdots \\ r(x_n,x_1) & \cdots & r(x_n,x_n) \end{pmatrix} \tag{3}$$

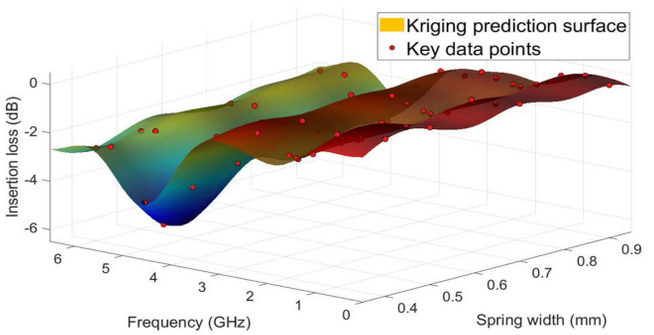


Fig. 1. (Color online) The effect of parameters on insertion loss as it varies with frequency.

$$r(x,x')=\exp\left(-\sum_{i=1}^{d}\theta_i\left|x_i-x_i'\right|^{\rho}\right) \tag{4}$$

where $r(x, x')$ is determined by the distance between points x and x'. When the distance between them is small, their correlation is high. Therefore, when selecting sample points in practice, as many sample points as possible should be chosen. In this study, ρ was set to 2, and a Gaussian correlation function was used because it is suitable for smooth and continuous response surfaces. θ in the equation is used to fit the uncertain parameters of the model, which is typically determined using the maximum likelihood estimation method.

In this work, the Kriging surrogate maps x = [w_1, w_2, w_3, w_4, w_5, f] to the positive insertion loss IL, where w_1-w_4 are structural variables, w_5 is the coating scheme, and f is frequency. The HFSS database included 480 simulation cases from single-factor sweeps and orthogonal multi-parameter samples. Each case was sampled at 20 frequency points, giving 9600 response records, which were divided into 80% training and 20% test data. A Gaussian correlation function with maximum-likelihood hyperparameter estimation was used, and model accuracy was evaluated by predicted-versus-HFSS scatter, residuals, R^2, and RMSE.

2.2. Kriging-IAGA Collaborative Optimization

The RF response cannot be reduced to independent one-factor effects. Single-factor simulations identified sensitive variables and feasible ranges, while orthogonal cross-parameter HFSS samples represented nonlinear coupling among spring width, bending angle, contact spacing, spring end distance, and coating scheme. Because the Kriging covariance is evaluated on the full input vector, the surrogate captures interaction effects across the joint design space. IAGA was then used to search this coupled surrogate efficiently.

For consistency, insertion loss is reported in this manuscript as a positive magnitude, IL = -S21(dB). Thus, a more negative S21 value in dB corresponds to a larger positive insertion loss. The fitness function minimizes this positive insertion-loss value:

$$Minimize f(x)=Insertion\ Loss\ (\mathrm{IL})=-20\log_{10}(|S_{21}|)\,(\mathrm{dB}) \tag{5}$$

In the present optimization, the primary fitness was IL at 4 GHz. This frequency was selected because the original relay exhibited its strongest loss fluctuation in the 3-4 GHz region, and 4 GHz is close to the upper part of the 1-5 GHz operating band where impedance discontinuity, current crowding, and coating penetration effects become more pronounced. The optimized design was therefore

selected using a stressed-frequency objective and was then verified over the full 1-5 GHz band. If the design requirement emphasizes uniform broadband behavior, the same framework can be extended to a broadband objective, such as the average IL, the maximum IL, or a weighted IL over all sampled frequencies.

$$F(x)=\frac{1}{1+f(x)} \tag{6}$$

The RF signal path was analyzed to identify the main factors affecting relay performance. Single-factor analysis and HFSS finite-element simulations were then used to determine the most influential optimization parameters, which served as constraints for IAGA. Because the optimization includes continuous structural variables and discrete material/process variables, hybrid encoding was used:

Continuous variables: represented by floating-point numbers (e.g., w = 0.5 mm).

Discrete variables: represented by integers or enumerated values (e.g., a = 1 for gold plating and a = 2 for silver plating).

Constraints are formulated to ensure feasibility, limiting the range of values for continuous variables and providing specific numeric values for discrete variables. If an individual violates the constraints, its fitness is reduced:

$$F_{\text{penalized}}(\mathbf{x})=F(\mathbf{x})\cdot\prod_{i=1}^{4}\max\left(0,1-\alpha\cdot\frac{|g_i(\mathbf{x})|}{\Delta g_i}\right) \tag{7}$$

α: Penalty Factor.

Δg_i: Constraint Boundary Width.

The population of size n, $P=\{x_1, x_2, ..., x_n\}$, is arranged in descending order of individual fitness values, and a nonlinear normalized geometric ranking function is applied, with the selection probability of individual i being:

$$\begin{cases} P(i)=q'(1-q)^{r-1} \\ q'=\dfrac{q}{1-(1-q)^n} \end{cases} \tag{8}$$

where q' is the selection probability of the best individual and r is the rank index of the individual.

Using this probability for roulette-wheel selection avoids reliance on absolute fitness values. This reduces the need for fitness scaling during population evolution and helps suppress premature convergence and evolutionary stagnation caused by the fitness-proportional selection strategy in traditional GA.

Consider the two-point arithmetical crossover operator applied to parent chromosomes. Let $w^1 = [w_1^1, w_1^2, \ldots, w_k^1, \ldots, w_n^1]$ and $w^2 = [w_1^2, w_2^2, \ldots, w_k^2, \ldots, w_n^2]$ be two chromosomes. When crossover is performed between positions i and j $(1 \le i < j \le n)$, the offspring chromosomes are generated as: $w^{1+t} = [w_1^1, \ldots, w_{i-1}^1, w_i^*, \ldots, w_j^*, w_{j+1}^1, \ldots, w_n^1]$, $w^{2+t} = [w_1^2, \ldots, w_{i-1}^2, w_i^{**}, \ldots, w_j^{**}, w_{j+1}^2, w_n^2]$. The newly inserted elements are derived from a convex combination:

$$\begin{aligned} w_k^* &= \alpha w_k^1 + (1-\alpha) w_k^2 \\ w_k^{**} &= \alpha w_k^2 + (1-\alpha) w_k^1 \end{aligned} \tag{9}$$

where $\alpha \in (0,1)$.

To accelerate convergence and suppress premature convergence, IAGA uses the following improved mutation operator. Let the individual chromosome be $w = [w_1, w_2, \ldots, w_k, \ldots, w_n]$, where the element $w_k \in [L_k, U_k]$ is the selected mutation, and the mutated value is:

$$W_k^* = \begin{cases} W_k + |\, r_2 (U_k - W_k) W_k \,|, & \text{if } r_1 < 0.5 \\ W_k - |\, r_2 (W_k - L_k) W_k \,|, & \text{if } r_1 \ge 0.5 \end{cases} \tag{10}$$

where r_1 is uniformly distributed on [0, 1], and r_2 follows a Gaussian distribution with a mean of 0.1 and a standard deviation of 0.2. If the mutated chromosome falls outside the feasible solution space, it is corrected as follows:

$$\begin{cases} \text{if } w_k^* < L_k, & \text{then } w_k^* = L_k \\ \text{if } w_k^* > U_k, & \text{then } w_k^* = U_k \end{cases} \tag{11}$$

The crossover probability P_c and mutation probability P_m control exploration and exploitation. Excessive P_c may disrupt useful schemata, whereas low P_c slows search; excessive P_m approaches random search, whereas low P_m limits diversity. In standard AGA, P_c and P_m may approach zero for high-fitness individuals, causing early stagnation. The improved adaptive strategy used here keeps nonzero probabilities for high-quality individuals to reduce premature convergence.

The adaptive crossover probability P_c and mutation probability P_m used in this study are defined as follows:

$$P_c = \begin{cases} P_{cl} - \dfrac{(P_{c1} - P_{c2})(f - f_{avg})}{f_{max} - f_{avg}}, & f' \ge f_{avg} \\ P_{cl}, & f' < f_{avg} \end{cases} \tag{12}$$

$$P_m = \begin{cases} P_{m1} - \dfrac{(P_{m1} - P_{m2})(f - f_{avg})}{f_{max} - f_{avg}} & f \ge f_{avg} \\ P_{m1} & f < f_{avg} \end{cases} \tag{13}$$

where f_{max} represents the maximum fitness of the current population, f_{avg} is the average fitness of the population, and f' is the larger fitness value of the two individuals selected for crossover. $P_{c1} = 0.9$, $P_{c2} = 0.6$, $P_{m1} = 0.1$, $P_{m2} = 0.01$. The improved algorithm ensures that the crossover and mutation probabilities of individuals with the maximum fitness in the population are not zero. Increasing P_{c2} and P_{m2} prevents high-quality individuals from being in a stagnation state. This allows the algorithm to escape local optima.

An elitism strategy was used to preserve the best current individual. If the next generation did not contain an individual better than the current best, the current best individual was copied into the next generation by replacing a low-fitness individual. This prevents loss of the best solution during crossover or mutation.

2.3. Grain Texture Optimization

In high-frequency electromagnetic fields, the electromagnetic properties of conductive materials, including permeability, dielectric constant, electrical conductivity, and electromagnetic-wave absorption/shielding ability, are strongly affected by grain size, grain-boundary density, and grain orientation [20, 21].

According to the skin effect, high-frequency currents are confined to a thin layer near the conductor surface, with the skin depth δ given by:

$$\delta = \sqrt{\frac{2}{\omega\mu\sigma}} \tag{14}$$

where ω is the angular frequency, μ is the permeability, and σ is the material's conductivity.

When the grain size is comparable to or larger than the skin depth, electron scattering at grain boundaries becomes a dominant loss mechanism, increasing the effective surface resistance. This can be described by the modified conductivity model accounting for grain boundary scattering:

$$\frac{1}{\sigma_{\text{eff}}} \approx \frac{1}{\sigma_{\text{bulk}}} + \frac{1}{\sigma_{\text{gb}}} \tag{15}$$

where σ_{eff} is the effective conductivity, σ_{bulk} is the bulk conductivity, and σ_{gb} is the conductivity limited by grain boundary scattering. Therefore, controlling the grain texture is essential for reducing insertion loss in high-frequency applications. In this study, the selection of coating materials and processes is intrinsically linked to grain texture control.

Grain texture is strongly affected by the deposition process. Compared with conventional electroplating, magnetron sputtering promotes dense and fine-grained coatings with lower roughness and fewer defects. This improves effective surface conductivity within the skin depth and helps confine RF current to the non-magnetic coating. As a result, field penetration into the ferromagnetic nickel layer is reduced, suppressing magnetic hysteresis and eddy-current losses. Thus, treating the coating process as an optimization variable implicitly accounts for beneficial microstructural effects.

2.4. Electromagnetic Mechanism of Insertion-Loss Reduction

At RF frequencies, current is concentrated near the conductor surface. Lower insertion loss requires a continuous low-impedance current path and reduced impedance discontinuity at the lead, spring contact, and contact region. Spring width, bending angle, spring end distance, and contact spacing jointly affect conducting cross section, current crowding, local inductance, and gap capacitance.

The coating scheme determines surface impedance and field penetration. When the conductive non-magnetic coating is thicker than the effective skin depth, most RF current remains in the silver or gold surface layer rather than entering the ferromagnetic substrate, reducing magnetic loss in the nickel-containing layer.

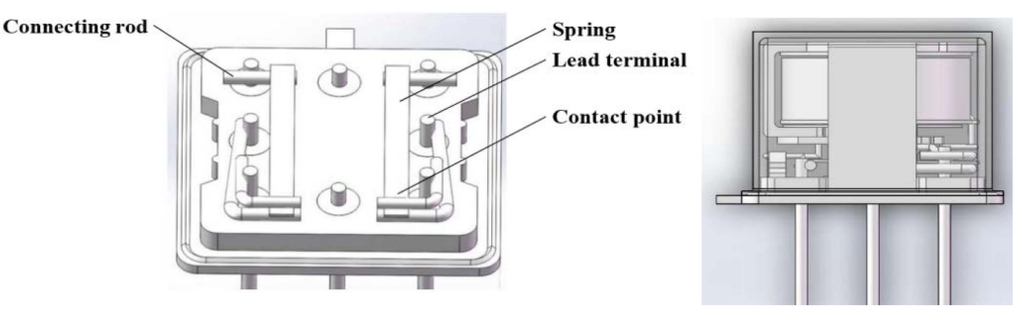


Fig. 2. (Color online) Schematic diagram of the relay's structure.

3. Engineering Experimental Research

3.1. Relay Structure and Model

The object investigated in this study was a TO-5 RF relay, whose three-dimensional model is shown in Fig. 2. The contact part of the RF relay mainly consists of a connecting rod, lead terminals, a base plate, a glass insulator, and a spring contact. It contains two sets of switching contacts. When the coil is excited by the rated voltage, the contacts switch; when the coil is de-energized, the contacts reset. This structure is suitable for RF signal switching in the range of 0 to 5 GHz.

3.2. HFSS Model and Engineering Procedures

The HFSS model reproduced the closed RF signal path of the relay used for insertion-loss evaluation. The geometry included the lead terminals, base plate, glass insulator, connecting rod, spring contact, contact gap region, and multilayer coating. The input and output RF terminals were defined as 50-ohm ports at the same reference planes used for the insertion-loss extraction, and S21 was used to calculate IL. The surrounding air region was terminated by an open/radiation boundary, while the metallic and coating regions were assigned finite material properties rather than ideal perfect conductors when conductivity or coating effects were compared.

Material properties were assigned according to the relay material system: finite conductivity was used for silver, gold, nickel-containing layers, and structural conductors; the glass insulator was assigned its dielectric constant and loss tangent; and the coating thickness was explicitly represented in the contact region. The frequency sweep covered the 1-5 GHz operating band, with additional points around the observed fluctuation frequencies. Adaptive meshing was refined near the spring contact, coating layer, contact gap, and port transitions to capture current crowding and field penetration.

Surface impedance and skin effect were represented by finite conductivity and coating thickness, while current crowding was captured by the three-dimensional contact geometry and local mesh refinement. Microscopic roughness and asperity-level DC contact resistance were not explicitly resolved because all compared designs used the same closed-contact state and similar preload; their influence was included in prototype measurements.

The engineering procedure is shown in Fig. 3. HFSS analysis identified five sensitive variables: spring width, contact bending angle, contact spacing, spring end distance, and coating scheme. These variables and frequency formed the Kriging input vector, and positive insertion loss IL was the output. Predicted, simulated, and measured

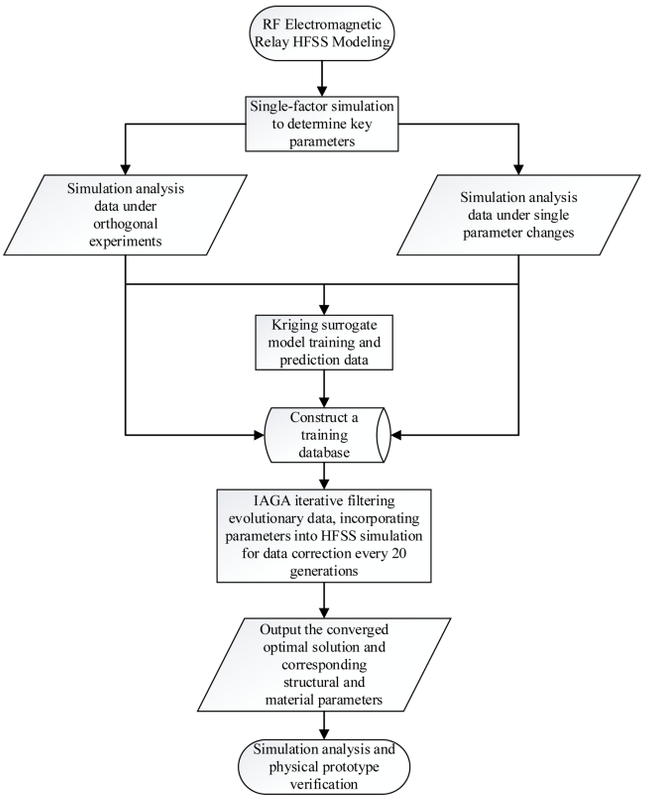


Fig. 3. Optimization plan flowchart.

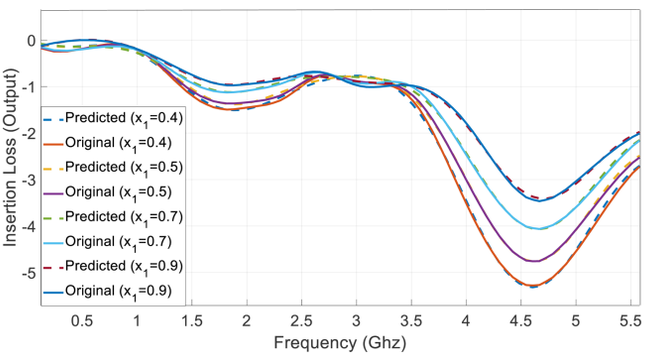


Fig. 4. (Color online) Comparison between model predicted data and simulation data.

values refer to Kriging, HFSS, and VNA results, respectively.

Fig. 4 compares the Kriging-predicted insertion-loss curves with HFSS simulation data for a representative single-factor sweep. Fig. 5 summarizes the validation of this single-factor surrogate. In Fig. 5(a), the black dashed line represents the ideal 1:1 relationship between predicted and HFSS-simulated values. The coefficient of determination $R^2 = 0.997$ and the root mean square error RMSE = 0.049 dB refer to this representative single-factor validation case, indicating high prediction accuracy

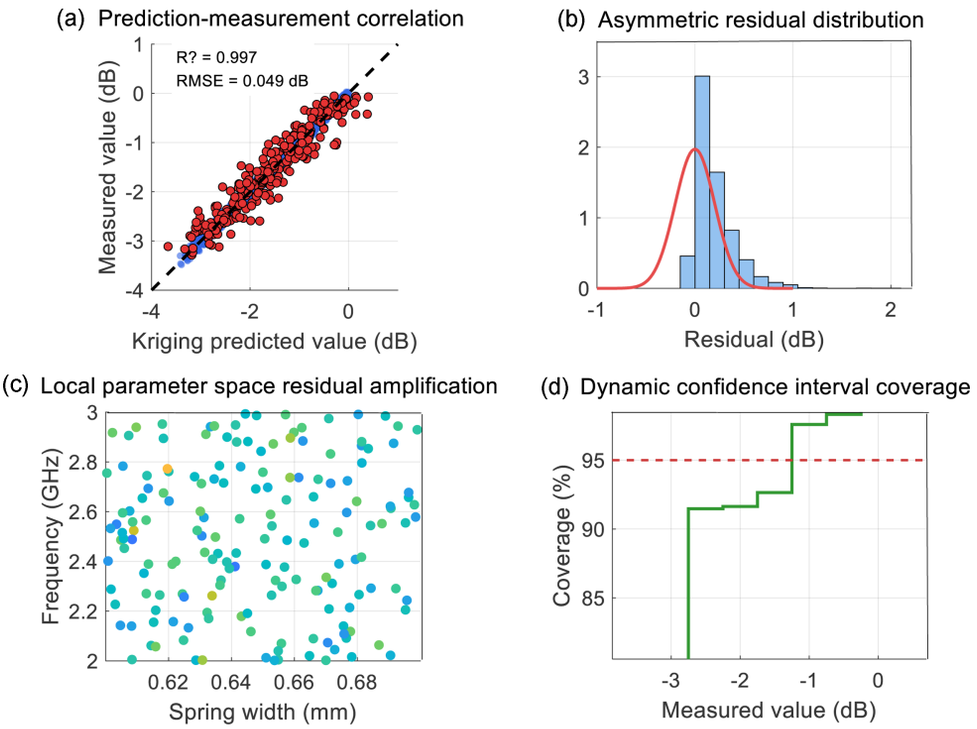


Fig. 5. (Color online) Performance of the surrogate model.

for the corresponding response surface.

The residual distribution characteristics are shown in Fig. 5(b). The standardized residuals exhibit a right-skewed distribution, which differs from the theoretical normal distribution curve. This asymmetry arises from the model's systematic underestimation in the spring width range of 0.6-0.7 mm (Fig. 5(c)). This phenomenon is related to the nonlinear response characteristics of relay contact pressure as spring width increases.

HFSS simulation data were used to train the surrogate model for insertion-loss changes caused by single-factor parameter variations, while the remaining responses were predicted by the surrogate model. This reduced the time required for repeated simulations and improved optimization efficiency.

Orthogonal cross-parameter HFSS simulations were added to the single-factor database. Since the Kriging covariance uses the full input vector, each chromosome response depends on combined changes in geometry, coating scheme, and frequency, allowing the surrogate to represent multi-parameter coupling.

Table 1. Range of key parameter variables.

Parameter	Range/Value	Coding type
Spring width (w_1)	0.70-0.85 mm	Real number
Contact bending angle (w_2)	75.0° -85.0°	Real number
Contact spacing (w_3)	1.90-2.40 mm	Real number
Spring end distance (w_4)	0.15-0.35 mm	Real number

The physical ranges of the optimization parameters were determined from the surrogate-model results, manufacturing constraints, and operating conditions. A hybrid encoding method was then used to construct the chromosomes, and the ranges of the four structural parameters are listed in Table 1.

For coating selection, the iron-nickel base layer, silver layer, and gold layer were evaluated considering shielding, skin depth, conductivity, oxidation resistance, and contact stability. Nickel improves mechanical strength but may introduce hysteresis and eddy-current losses if RF fields penetrate into it. Gold provides stable conductivity and oxidation resistance, while silver offers higher conductivity but requires protection against sulfide formation. Therefore, the selected silver scheme used a thin sputtered gold protective layer to prevent oxidation.

The coating thickness must exceed the skin depth to prevent RF current from entering the nickel layer and increasing contact impedance. In the 1-5 GHz band, the required thickness was greater than 2.5 μm. Simulations showed little additional insertion-loss change above 3 μm, so two manufacturable schemes were retained: 3 μm gold plating and 3 μm silver plating with a thin gold protective layer. The coating variable was encoded as $w_5 = 1$ for gold and $w_5 = 2$ for silver; thus, a chromosome is $w = [w_1,$

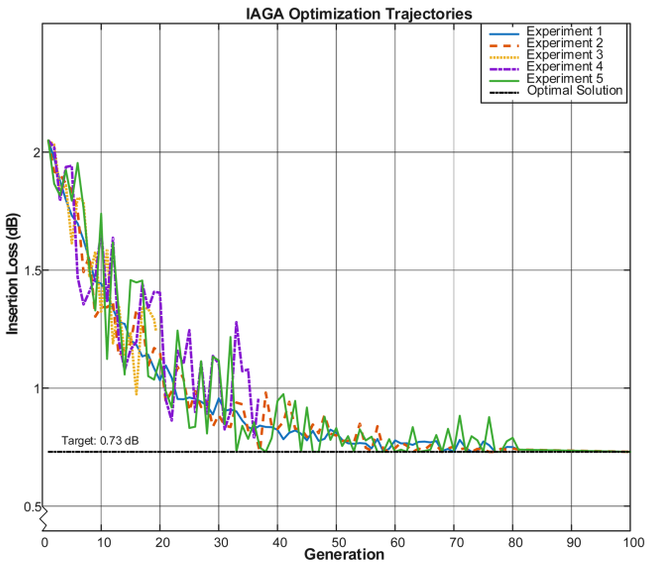


Fig. 6. (Color online) Evolution of the positive insertion-loss objective, IL = -S21(dB), during optimization.

w_2, w_3, w_4, w_5].

Fitness was evaluated by surrogate-predicted IL. To reduce surrogate uncertainty, the current best individuals were re-simulated in HFSS every 20 generations and added to update the Kriging model. IL at 4 GHz was used as the objective, and the final design was verified over 1-5 GHz.

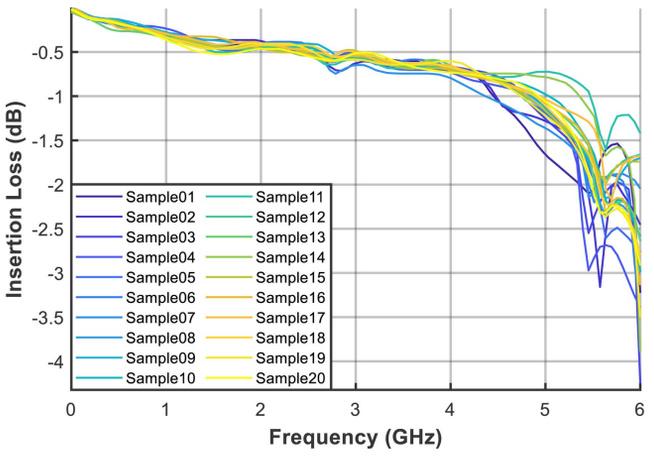


Fig. 7. (Color online) Measured insertion-loss curves of the optimized prototype.

Table 3. Final optimization plan parameters.

Parameter	Value
Spring width	0.82 mm
Contact bending angle	81.5°
Contact spacing	2.15 mm
Spring end distance	0.25 mm
Coating layer	Silver plating 3 μm + thin gold protective layer

Fig. 6 shows five evolutionary runs, with the third run reaching the optimum fastest at generation 33. Table 2 compares Kriging-IAGA, Kriging-SGA, and Kriging-PSO over 10 independent MATLAB trials. All algorithms used the same bounds, surrogate database, population/swarm size of 50, maximum 100 generations/iterations, and convergence criterion of no best-fitness improvement for 20 generations/iterations. IAGA used P_{c1} = 0.9, P_{c2} = 0.6, P_{m1} = 0.1, and P_{m2} = 0.01; SGA and PSO used standard MATLAB toolbox operators and default remaining settings. Curve fluctuations reflect candidate exploration, while elitism preserves the historical best solution.

3.3. Verification of the optimized prototype

The optimal chromosome obtained by Kriging-IAGA was w = [0.82 mm, 81.5°, 2.15 mm, 0.25 mm, 2], corresponding to the final key parameters of the RF relay model, as listed in Table 3.

The optimized prototype was fabricated according to the chromosome parameters in Table 3. To account for manufacturing tolerances, 20 prototypes with structural

Table 4. Product performance after optimization

Frequency	IL of the original product	IL of the optimized product	Improvement rate
1.14 GHz	0.51	0.29	43.1%
1.79 GHz	0.52	0.41	21.1%
2.73 GHz	1.17	0.57	51.3%
3.38 GHz	1.93	0.644	66.6%
4.03 GHz	2.03	0.712	64.9%
4.78 GHz	0.884	0.98	-10.8%
5.79 GHz	3.19	2.26	29.1%

Table 2. Performance comparison of three algorithms.

Algorithm	Number of simulations	Generations to converge to a local optimum	Minimum successful convergence generations	Expected optimal solution (dB)
Kriging-IAGA	10	0	33	0.73
Kriging-SGA	10	2	76	0.94
Kriging-PSO	10	6	60	0.85

parameters within an 8% tolerance range were selected for insertion-loss testing. The RF measurement was conducted with the relay in the same closed-contact state used in the HFSS model.

A total of 25 contact sets were measured, with IL calculated as -S21 (dB). The optimized relay maintained IL below 1.8 dB within 1-5 GHz, and the main fluctuation shifted from 3-4 GHz to about 5.5 GHz. The measured spread was approximately 0.2 dB, with only a small local degradation near 4.78 GHz.

The final product performance is summarized in Table 4.

Note: The frequency points in the table were selected from representative fluctuation points in the original insertion-loss curve.

The improvement rate is defined as $(IL_{original} - IL_{optimized})/IL_{original} \times 100\%$; therefore, a negative value indicates a local degradation at that frequency point.

At 4.78 GHz, the optimized product showed a small local increase from 0.884 to 0.98 dB. This was likely caused by the upward shift of the loss fluctuation after suppression of the main 3-4 GHz peak, indicating overall broadband improvement with a limited local trade-off.

4. Conclusion

Optimization algorithms are increasingly important in electromagnetic-shielding and RF-device design. However, traditional optimization methods remain challenging for insertion-loss optimization because repeated simulations and prototype fabrication are time-consuming, and the target response is difficult to predict under varying input conditions.

This paper proposes a Kriging-IAGA strategy combining material/process selection with multi-parameter optimization. The surrogate learns insertion-loss trends from limited HFSS data, and IAGA identifies the optimal structural and coating combination. The optimized geometry reduces impedance discontinuity and current crowding, while the coating lowers surface impedance and shields the ferromagnetic layer.

Future work should extend Kriging-IAGA to other RF relay indices such as isolation, include microstructural variables such as grain size and orientation, and reduce the simulation or measurement data required for surrogate training.

References

[1] P. F. Wilson, J. W. Adams, and M. T. Ma, Proceedings of the IEEE **74**, 112 (1986).
[2] M. Peng and F. Qin, Journal of Applied Physics **130**, 22 (2021).
[3] H.-C. Chow, P. Chatterjee, K.-H. Lin, and W.-S. Feng, J. Magn. **22**, 275 (2017).
[4] Sh. U. Pulatov, U. Sh. Sabirova, Z. T. Khakimov, A. S. Shamsiev, and J. D. Isroilov, in 2020 International Conference on Information Science and Communications Technologies, IEEE, 1 (2020).
[5] Q. Li, W. Cao, J. Ding, J. Fang, J. Sun, and C. Guo, in 2022 International Conference on Microwave and Millimeter Wave Technology, IEEE, 1 (2022).
[6] T. Singh, J. Comput. Electron. **14**, 167 (2014).
[7] L.-B. Jing, J. Li, and X. Ding, Antennas Wirel. Propag. Lett. **24**, 1934 (2025).
[8] Z. Ke, J. Deng, Y. Xu, X. Zhao, and Q. Li, in 2024 6th International Conference on System Reliability and Safety Engineering (SRSE), 246 (2024).
[9] Y. Chen, F. Yu, L. Chen, G. Jin, and Q. Zhang, Energy **334**, 137730 (2025).
[10] F. Passos, R. Gonzalez-Echevarria, E. Roca, R. Castro-Lopez, and F. V. Fernandez, in 2015 International Conference on Synthesis, Modeling, Analysis and Simulation Methods and Applications to Circuit Design (SMACD), IEEE, 1 (2015).
[11] B. Xia, Z. Ren, and C.-S. Koh, IEEE Trans. Magn. **51**, 1 (2015).
[12] Y. Pang, S. Zhang, Y. Jin, Y. Wang, X. Lai, and X. Song, Swarm Evol. Comput. **88**, 101586 (2024).
[13] D.-W. Kim, N.-S. Choi, K. K. Choi, H.-G. Kim, and D.-H. Kim, J. Magnetics **19**, 78 (2014).
[14] S. H. Oh, D. K. Lim, J. Magnetics **30**, 203 (2025).
[15] S. Kasdorf, J. J. Harmon, and B. M. Notaros, IEEE Open J. Antennas Propag. **5**, 474 (2024).
[16] J. M. Johnson and Y. Rahmat-Samii, in 1996 IEEE Aerospace Applications Conference. Proceedings, IEEE **1**, 87 (1996).
[17] J. Palecek, M. Vestenicky, P. Vestenicky, and D. Ticha, in 2012 EL-EKTRO, IEEE, 79 (2012).
[18] Y.-M. You and D.-W. Chung, J. Magnetics **22**, 423 (2017).
[19] M. Marseguerra, E. Zio, and S. Martorell, Reliab. Eng. Syst. Saf. **91**, 977 (2006).
[20] C. Shao, C. Ding, Y. Liu, Y. Ma, L. Zhang, X. Ren, S. Wu, B. Zhong, G. Wen, and X. Huang, Chem. Eng. J. **466**, 143162 (2023).
[21] N. Wang, R. Yang, W. Yao, J. Xu, and X. Wen, J. Mater. Sci. Technol. **28**, 833 (2012).